Tunnelling and Underground Space Technology 168 (2026) 107181

Contents lists available at ScienceDirect

Tunnelling and Underground Space Technology incorporating Trenchless Technology Research

journal homepage: www.elsevier.com/locate/tust

Automated 3D reconstruction of high-resolution images for tunnel inspection and monitoring purposes

Saduni Melissa Dahanayaka [a,*], Adriàn Riquelme Guill [b], Alessia Vecchietti [c], Matteo Del Soldato [a]

[a] Earth Sciences Department of the University of Florence, Via La Pira 4 Florence 50121, Italy
[b] Civil Engineering Department, University of Alicante, Carretera San Vicente del Raspeig s/n 03690 San Vicente del Raspeig – Alicante, Spain
[c] pizzi terra S.r.l., Via Del Fornaccio 46, Bagno a Ripoli (FI) 50012, Italy

ARTICLE INFO

Keywords:
Tunnel
Inspection
Monitoring
Image processing
3D image reconstruction

ABSTRACT

The paper presents an automated tool for reconstructing a three-dimensional (3D) model of tunnel infrastructure using high-resolution images. In the last decades, image acquisition and survey with mobile systems, *i.e.*, sensors mounted on vehicles, have seen major advancements in the field of infrastructure inspection. Traditionally, image mosaicking has been addressed by means of photogrammetry approaches, but this methodology has not been suitable for specific high-resolution image data acquired with an innovative mobile mapping system. The developed methodology assigns spatial coordinates to each pixel of the acquired images, allowing the creation of a textured 3D geometric model of the tunnel surface. To this aim, the cross-sectional geometry of the tunnel was first parametrised using best fitting methods, simulating the tunnel shape as an ellipse in a proper coordinate system. The resulting 3D reconstruction from imagery offers a comprehensive and highly detailed representation of structural elements, enabling direct identification and evaluation of concrete defects, visible alterations, and millimetric cracks. This procedure facilitated the assessment of crack dimensions and their potential impact. The study opens new opportunities for the digitalization of tunnel inspection practices. The 3D scaled high-resolution imagery can enable easier detection, mapping and quantitative classification of defects. The obtained digital model, combined with other techniques, *e.g.*, AI detection algorithms and real-time monitoring data, can provide a comprehensive assessment of the actual state of tunnels. Finally, the method supports temporal monitoring, allowing the comparison of subsequent surveys to observe structural changes over time.

1. Introduction

Geotechnical and structural monitoring and inspection of existing infrastructures have gained a great prominence in Italy. Tunnels, roads and bridges have been in service for many years experiencing different stages of decay and deterioration, some of them approaching to the end of their operating life (Barla et al., 2021; Beltrami et al., 2021). New regulations for the inspection, monitoring, and maintenance of tunnels and bridges were issued by the Italian Ministry of Infrastructure and Transport, the Linee Guida Gallerie and Linee Guida Ponti (MIT, 2022a, b), and a massive inspection plan has been carried out to guarantee a constant maintenance and safe condition of existing infrastructures. The new guidelines introduce an innovative and multi-level approach for safety and risk evaluation, which defines the inspection activity planning: i) Level 0 represents the preliminary infrastructure state of consistency and fundamental features collection; ii) Level 1 delineates the first visual inspection activity; and iii) Level 2 is necessary for the definition of an Attention Class. By assigning this Attention Class, it is feasible to conduct a safety assessment of the structure and schedule further inspections, interventions, and monitoring strategies through the subsequent levels (from Level 3 to 5) which focus on structure safety evaluation (Salomone et al., 2023). One of the main processes for infrastructure management and risk assessment is the *Structural Health Monitoring* (Brownjohn, 2007): a combination of different measurement systems, including Non-Destructive Inspection/Evaluation (NDI/E) and remote sensing methods, allow it to pursue its objectives.

Over the past few years, non-invasive techniques, *e.g.*, Unmanned Aerial Vehicles (UAV), LiDAR (Light Detection and Ranging) and photogrammetry, have been widely used and combined to build measurable 3D models (*e.g.*, Chen et al., 2019; Gaspari et al., 2023;

* Corresponding author.
E-mail address: melissa.dahanayaka@unifi.it (S.M. Dahanayaka).

https://doi.org/10.1016/j.tust.2025.107181
Received 20 January 2025; Received in revised form 11 September 2025; Accepted 14 October 2025
Available online 21 October 2025

Mandirola et al., 2022; Pepe and Costantino, 2021; Zollini et al., 2020) or Digital Twins (*e.g.*, Mahmoodian et al, 2022; Machado and Futai, 2024) of the infrastructure. The digital model can be then investigated directly in the office for inspection and monitoring purposes. As an example, UAVs have facilitated the adoption of cost-effective and non-destructive evaluation methods for the inspection and monitoring of existing bridges (Pinto et al., 2020), even in inaccessible areas and challenging environments. Specific visualization and data management software and platforms have been developed and already used by engineering companies for bridge inspection and asset management purposes, *e.g.*, *ARGO* asset management platform (Buggiani et al., 2024).

Inspection activities on existing tunnels have mainly been performed on-site by technicians through direct visual assessment from elevating platforms, causing traffic interruption and time-consuming operation. Moreover, it can be affected by inaccuracies due to the subjective evaluation by the inspector, leading to partially or totally missing estimations. In the last decades innovative scanning technologies, *e.g.*, mobile mapping systems (Foria et al., 2023; Iacobini & Pranno, 2023), and data processing methods have been studied and developed for tunnel damage investigation and deformation monitoring. Other examples of 3D tunnel surface reconstruction take advantage from LiDAR data (Farahani et al., 2019; Paar and Kontrus, 2006), photogrammetric approaches and Structure from Motion (SfM) techniques (Attard et al., 2018; Scaioni et al. 2014). Static LiDAR often faces challenges in capturing high-resolution texture data inside poorly lit, curved tunnels. On the other hand, many existing mobile LiDAR systems operate at lower resolution, limiting sub-millimetric defect detection (Soudarissanane et al., 2011, Ding et al., 2024). Photogrammetric approaches based on SfM techniques rely on overlapping multiple images captured from various angles to create a true-to-scale 3D model with detail (Chaiyasarn et al., 2016). The application of photogrammetry on tunnels poses logistical challenges and safety concerns in addition to difficulties to manage data recorded in this peculiar environment.

The 3D representation is necessary to provide a reliable and immersive visualization of the tunnel, supporting inspection activities through innovative scanning systems and advanced data management procedures. Moreover, the digitalization of infrastructure data enables the creation of a historical repository of tunnel conditions, which is particularly relevant for infrastructure asset management in Italy.

While the traditional inspection, needing access to all parts of a tunnel for comprehensive imaging, may require traffic closures, mobile scanning approaches overcome this issue. At present, acquisition methods to optimize time efficiency and achieve the highest resolution of image data have been studied (Doreau-Malioche et al., 2023). The system named *Tunnelings*, proposed by Gavilán et al. (2013), is composed by cameras, optics and laser line projectors and allows acquiring 3D data and two-dimensional (2D) images with 1 mm resolution for a 12 m long tunnel section, at a speed up to 30 km/h. Huang et al. (2017) designed the *MTI-100*, an image acquisition device for subway tunnel inspection composed by high-resolution line-scan cameras and lighting, reaching a resolution of 0.3 mm/pixel at a driving speed of 5 km/h. Liao et al. (2022) presented a multi-sensor system integrating line cameras and laser scanner sensors to provide 0.2 mm/pixel accuracies running at speeds up to 80 km/h. Mobile acquisition Services for inspection purposes are available on the market for both railway and road tunnels, offering multi-sensor systems to acquire 3D point cloud data, high-resolution images and thermal images, *e.g.*, *TS4* system by SPACETEC (Cereyon et al., 2019); *ARCHITA* by ETS S.r.l. integrates Ground Penetrating Radar (GPR) sensors to investigate railway infrastructures (Foria et al., 2019). These hardware systems are well-established; despite this, they often provide only 2D visualizations of the inspected surfaces and assume near-circular geometries, limiting adaptability to different tunnel cross-sections.

TunnelEye project (European Commission, 2022) was implemented under the *RIMA European Union's Horizon 2020* research and innovation programme. It dealt with the development of a prototypical kinematic image acquisition hardware and the preliminary exploration of defect identification through Artificial Intelligence (AI) algorithms, aimed at seeking for 0.5 mm cracks. Some of the Authors joined the project and focused on obtaining high resolution 2D pictures to improve the crack detection. Nonetheless, the development of robust algorithms for 3D reconstruction was not the primary objective of the research. It is expected that the combination of 2D images and 3D data can have a significant impact on the data visualisation and presentation. Thanks to the acquisition of high-resolution images, it is possible to detect very small deteriorations on tunnel surfaces, *e.g.*, sub-millimetric cracks and micro-defects. However, such accurate identification is only achievable if both geometric accuracy and texture integrity are preserved.

In this paper, we address the identified gap, *i.e.*, the lack of an automated 3D reconstruction procedure, by proposing a novel modelling approach that bypasses traditional photogrammetry for image post-processing. The proposed approach combines: (*i*) ellipse-fitting to flexibly model polycentric cross-sections, and (*ii*) an optimization algorithm to robustly calibrate sensor position for accurate image-to-geometry mapping. An algorithm for automated 3D reconstruction from high-resolution images and LiDAR data acquired via mobile mapping systems has been designed. It enables accurate modelling across diverse tunnel geometries, supports sub-millimetric defect detection, and reduces the need for manual post-processing. Compared with workflows that rely solely on 2D for crack detection, the proposed method integrates geometric reconstruction and rectification at an earlier stage.

The analysed images were acquired through the mentioned *TunnelEye* system. Specifically, high-resolution black and white images of tunnel linings were captured through this mobile system (Fig. 1) composed by two image sensors, lamps for a correct illumination of the tunnel surface and positioning systems, *i.e.*, odometer and inertial sensors. Hardware to manage the camera and to store collected data, *i.e.*, acquisition PC and power system, are placed inside the vehicle. Cameras and lamps are fixed on a frame, mounted on the top of a trailer, with a total view angle of approximately 120°, which can be rotated at different angles to capture different areas of the tunnel. The speed of execution, to obtain the best resolution of the acquired images in a dark environment, needs to be maintained at 10–20 km/h. The two image sensors are linear cameras and optics with specifications optimized to capture high-quality images in movement inside tunnels with poor lighting conditions. The pixel number for each line is 6144, and the pixel size is 7 μm x 7 μm. Each

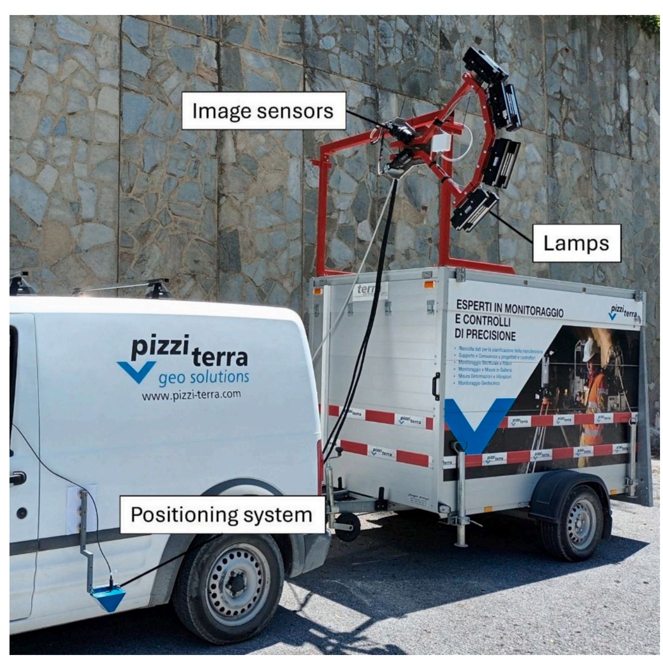

Fig. 1. High-resolution image acquisition system and components disposition.

lens has a focal length of 35 mm, image field diameter of 43 mm and a view-angle of 63,1°. The preference and choice of linear cameras with respect to area cameras in tunnel imaging is primarily due to their adaptability to consistent lighting given by the line lamps. In a few passes of the vehicle with the instrumentation mounted on the top, it is possible to reconstruct the whole tunnel surface, including walls and ceiling, with potential no traffic interruption.

2. Methodological approach

Tunnels can have various cross-sectional geometries, including circular, horseshoe, rectangular, and arch types, each chosen based on specific structural requirements, geological conditions, excavation method, and functional necessities. The work focuses on the representation of acquired linear images on a 3D model approximating the geometry with an ellipse that defines the tunnel shape. This simplification was adopted based on the typical geometries encountered in road tunnels, particularly those excavated with tunnel boring machines (TBMs). The elliptical approximation provides a balance between modelling accuracy and computational simplicity, allowing a reliable geometric reference for image projection and defect localization. The 3D representation of a tunnel from 2D high-resolution linear images was accomplished through the reconstruction of a 3D geometric model coded in a Matlab-based (The MathWorks Inc, 2024) tool, which automatically assigns the colour information to the corresponding point with (x, y, z) coordinates (Fig. 2). The methodology involves two distinct optimization stages: (*i*) ellipse fitting to the tunnel cross-section, performed by minimizing the Mean Squared Error (MSE) using the *fminsearch* function (Lagarias et al., 1998), a nonlinear least squares approach, and (*ii*) sensor position and orientation estimation, carried out by solving a system of trigonometric equations through genetic algorithms (Golberg, 1989), using a fitness function defined as the Root Mean Squared Error (RMSE) of the residuals between observed and calculated target coordinates.

After defining the tunnel cross-section geometry via ellipse fitting, geometric parameters of the sensor were estimated using known coordinates of several reference elements visible on the tunnel surface. Having determined these parameters, the coordinates of each pixel were calculated and automatically assigned to the image, producing a high-resolution 3D point cloud.

2.1. Tunnel cross-section geometry definition

A geometric ellipse fitting was implemented to adapt an ellipse to a cross-section obtained from any available geometric data of the tunnel, *e.g.*, point clouds, polylines. In this work, the best fitting was applied on cross-sectional slices extracted by point cloud data, with a width of 0.1 m along the z-axis. An ellipse can be fitted to the extracted cross-section points using a least-squares optimization method. The general equation of an ellipse is:

$$\frac{(x-x_0)^2}{a^2}+\frac{(y-y_0)^2}{b^2}=1 \tag{1}$$

And the parametric equations of a rotated ellipse, describing how coordinates x and y change as θ angle varies, are given by:

$$\begin{cases} x(\theta) = x_0 + a\cos\theta\cos\phi - b\sin\theta\sin\phi \\ y(\theta) = y_0 + a\cos\theta\sin\phi + b\sin\theta\cos\phi \end{cases} \tag{2}$$

where a is the semi-major axis, b is the semi-minor axis, (x_0, y_0) are the coordinates of the centre of the ellipse, θ is the angular parameter varying from 0 to 2π, and ϕ is the rotation angle of the ellipse. An initial estimation for the ellipse parameters was set based on the mean and range of the point cloud cross-section for the axes and ellipse centre coordinates, respectively. The *fminsearch* Matlab function was employed to minimize the Mean Squared Error (MSE) between the extracted points and the parametric form of the ellipse, adjusting the parameters iteratively, as:

$$MSE = \frac{1}{n}\sum_{i=1}^{n} d_i^2 \tag{3}$$

where d_i is the Euclidean distance from point (x_i, y_i) to the fitting ellipse, and n is the number of points belonging to the cross-section.

2.2. Sensor parameters optimization

Three-dimensional coordinates of each image pixel were calculated by developing a geometric model that determined the sensor position within the tunnel cross-section and its viewing angle relative to the captured sector, *i.e.*, wall and ceiling. The model was calibrated by identifying targets or elements of known coordinates on the wall in both the image and the point cloud. The required parameters of the model, which are referenced with respect to the centre of the ellipse (Fig. 3), are the position of the sensor S, the position of the target T, the distance between the sensor and target R', the distance between the centre and the target R, the angle of the sensor δ, and the angle of the target position relative to the horizontal α. The view angle of the camera is defined by the arc segment between the angles β_0 (angle between the horizontal direction and the lower limit angle of the camera view) and β_1 (angle between the horizontal direction and the upper limit angle of the camera view), while β_T represents the camera angle of the target. The geometric centre of the tunnel section is set as $(0,0)$.

A system of two equations was defined to determine the unknown parameters of the model. The system of equations is as follows:

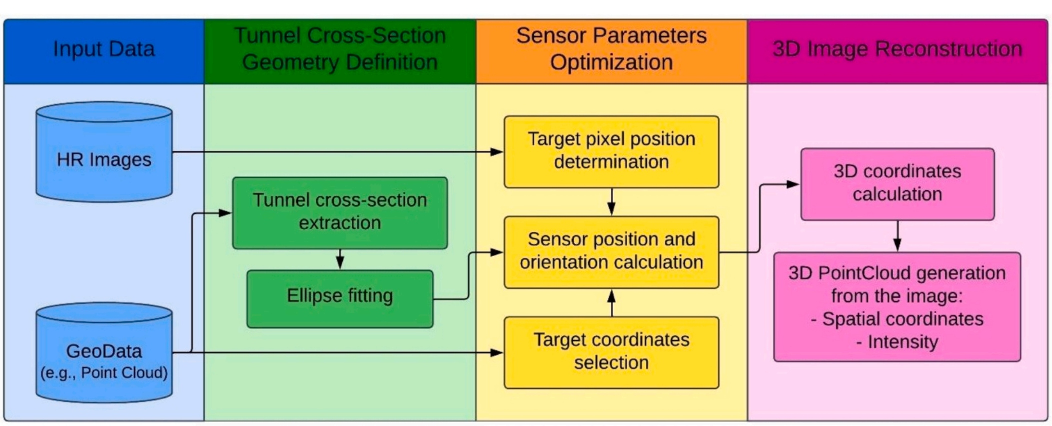

Fig. 2. Methodology workflow.

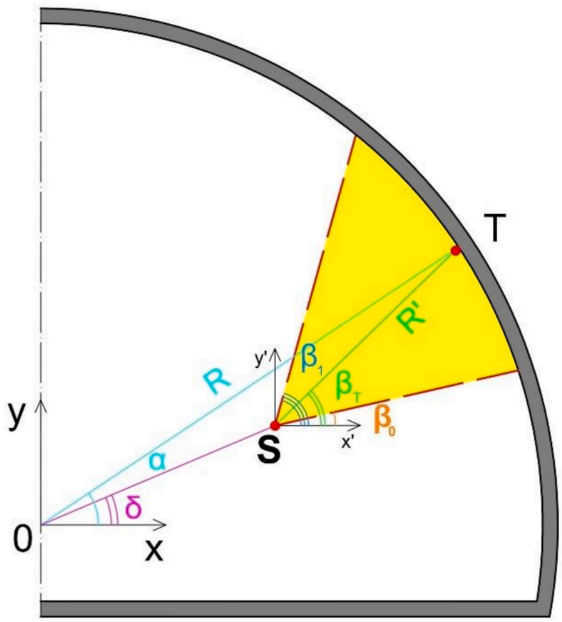

Fig. 3. Geometric model of the tunnel half cross-section showing the position of the sensor, the position of the target and the respective angles and distances. The origin of the reference system is set at the geometric centre of the tunnel cross-section. The x-axis points horizontally, while the y-axis is oriented vertically upward. The sensor S is located above the tunnel centreline.

$$\begin{cases} x_T = x_S + R'cos\beta_T \\ y_T = y_S + R'sin\beta_T \end{cases} \tag{4}$$

where the dependent variables are the following:

$$R' = R\frac{sin(\alpha - \delta)}{sin(\pi + \delta - \beta_T)} \tag{5}$$

$$\delta = arctan\frac{y_S}{x_S} \tag{6}$$

$$\beta_T = \beta_0 + \frac{\beta_1\text{-}\beta_0}{n}i \tag{7}$$

The system of equations for the calculation of target coordinates (4) and the equations of dependent variables (5)-(6) were designed to correlate various trigonometric functions for the variables of the model, ensuring a comprehensive correlation. The equation for the calculation of the angle between the horizontal direction and the target (7) specifically describes the angles of the acquisition sensor. The input values are the coordinates of the target (x_T, y_T), which form the angle α, radius R, the number of pixels on an image line n, and the pixel i of the target element on the image, where $0 < i < n$. The output values are the coordinates of the sensor (x_S, y_S), which allow the calculation of the angle δ, while distance sensor-target R' and rotation angle of the acquisition sensor β_T are dependent variables. Therefore, the unknown values are (x_S, y_S) coordinates and the angle β_0, which are major to the number of equations.

The system of equations defined for determining the unknown parameters of the model can be adapted to an elliptical geometry cross-section. In this adaptation, radius R used in the equations is calculated as the radius of the ellipse at a given angle α, corresponding to ϕ angle in (2). This modification allows for parameter determination within the elliptical framework. For an ellipse centred at (X_0, Y_0) with semi-major axis a and semi-minor axis b, the radius at an α angle is given by:

$$R_{ellipse} = \frac{ab}{\sqrt{(bcos\alpha)^2 + (asin\alpha)^2}} \tag{8}$$

Given the complexity of the non-linear problem and the difficulty in finding a solution due to the number of unknown parameters, genetic algorithms were selected for the optimization process because of their robustness. The genetic algorithm function, given by the *Global Optimization Toolbox* in Matlab, was implemented to solve the problem. A certain number of target points is necessary for model calibration to ensure better convergence to the solution. These targets can be selected, for example, from a point cloud, or any geo-referenced facility inventory, and must be detectable in the image. The fitness function adopted for the genetic algorithm is the RMSE of the residuals between the observed target positions and the coordinates calculated by the model. It quantifies the misfit between actual and modelled target positions and is minimized by adjusting the sensor parameters.

2.3. 3D image reconstruction

Optimal parameters for sensor position (x_S, y_S) and the angle β_0 extracted out of the genetic algorithm process allow to calculate (x, y) coordinates for each pixel P of the image; (x, y) coordinates are derived from the elliptical parameters, while the angle β_P can be calculated and the distance sensor-wall R' computed for each angle α with the following equation (sine rule):

$$\frac{R'}{sin(\alpha - \delta)} = \frac{R_{ellipse}}{sin(\pi + \delta - \beta_P)} \tag{9}$$

The coordinates are calculated based on R' and the angle β_P, imposing a specific constraint to R'. This process ensures that the computed coordinates are accurately placed on the ellipse, reflecting the correct geometry of the cross-section and the optimized position of the camera sensor. Finally, 3D coordinates can be assigned to each image pixel, where coordinates are derived from the elliptical parameters, while z coordinate is linearly spaced to represent the length of the considered image, *i.e.*, 20 m. Pixel intensity values are normalized and combined with coordinates to create a point cloud vector feature, which includes spatial and intensity information.

3. Dataset collected in a test area

Inspection surveys were conducted on some highway tunnels in central Italy characterized by visible structural deteriorations and cracks. These tunnels have a horse-shoe geometry section and exhibit longitudinal and cross-sectional cracks up to 5 mm thick, which were identified as construction defects and needed consolidation works. The presence of damage and cracks made necessary a complete inspection of the tunnel including acquisition of geo-referenced point cloud and image survey.

Two different kinds of dataset were acquired from two distinct acquisition systems (Fig. 4): high-density point clouds, acquired by the Mobile Laser Scanning (MLS) system, and high-resolution images, captured by the mobile image capturing system *TunnelEye*. The point cloud was used to derive the cross-sectional geometry through geometric fitting algorithms and to extract the coordinates of targets and known wall elements for model calibration and sensor position identification.

3.1. Point cloud data

The MLS system used for the point cloud acquisition is composed of a dual laser scanner system, positioning system, 360-degree cameras for the RGB information and inertial system, all installed on a vehicle. The scanning was carried out at speeds of approximately 30–40 km/h,

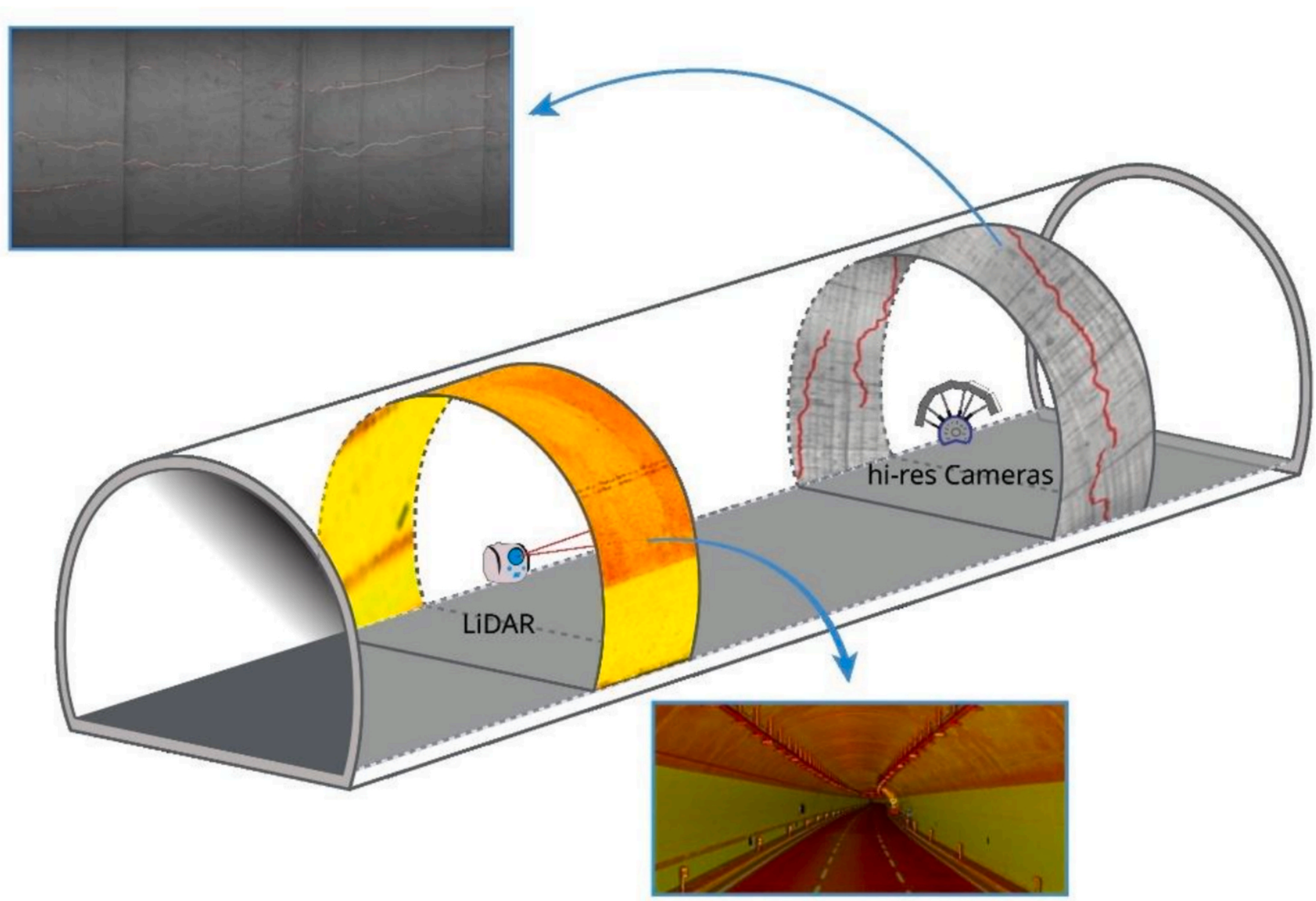

Fig. 4. Lidar scanning and high-resolution images acquisition representation.

allowing the collection of a point cloud with a density of approximately 3000 points/m^2, equivalent to one point every 2 cm x 2 cm, roughly. For a better georeferencing accuracy, the resulting point cloud was georeferenced through Ground Control Points (GCPs) on the walls and targets outside the tunnels collected by a GPS (Global Positioning System) for having the latitude and longitude coordinates. In the context of these analyses, the point cloud was manually cleaned of components not belonging to the tunnel surface, including the roadway, signage, support structures and lighting installations. Additionally, any potential noise that can impact the tunnel design profile was removed using Statistical Outlier Removal (SOR) filters in Cloud Compare software (Girardeau-Montaut, 2024) (Fig. 5).

3.2. High-resolution images

To collect high-resolution images of the whole tunnel surface, four image captures (Fig. 6) were performed with the *TunnelEye* system: left and right wall (first and second run into the tunnel, respectively) and left and right ceiling (third and fourth run into the tunnel, respectively). This approach resulted in n. 8 images that effectively represent the tunnel wall internal profile. The two cameras are labelled as *Cam_01* and *Cam_02*. The number of shots was determined according to the

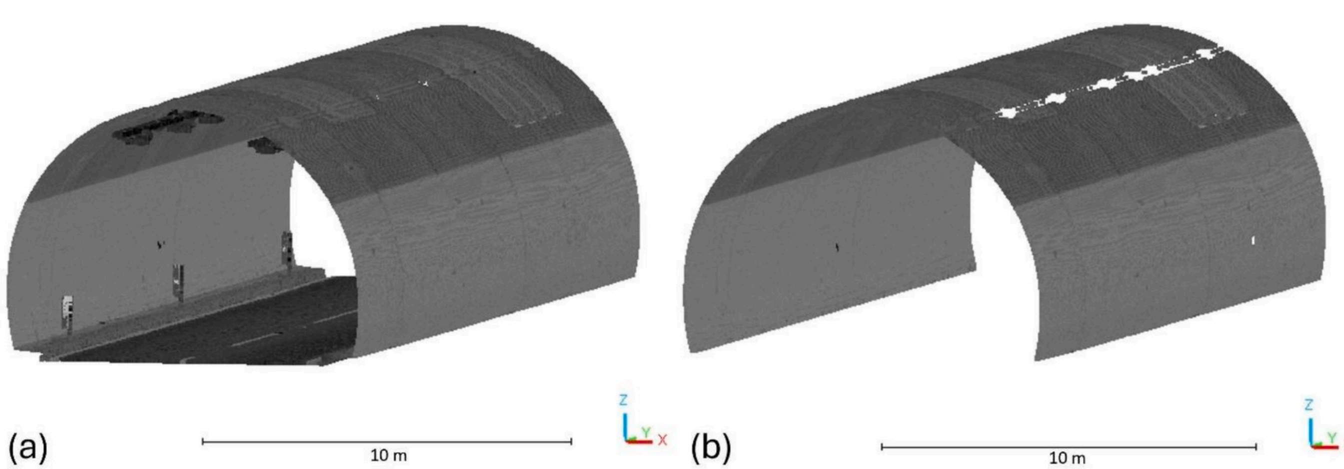

Fig. 5. 3D point cloud of a tunnel block acquired by MLS system: (a) original point cloud, (b) cleaned point cloud representing only the tunnel surface.

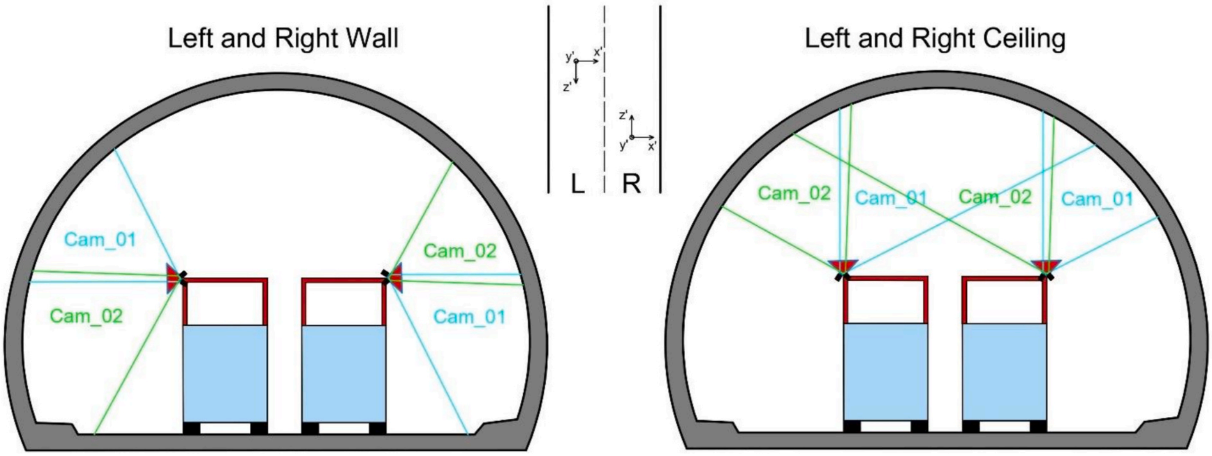

Fig. 6. Schematic of image acquisition with n. 2 cameras (Cam_01 and Cam_02) on the tunnel cross-section for Left and Right Wall and Left and Right Ceiling.

dimensions and geometry of the tunnel, to capture images of each sector, *i.e.*, wall and ceiling, with a certain overlap, providing comprehensive coverage and enough redundancy for image stitching purposes. The runs were executed with a focus on minimizing the impact of lighting variations and maintaining consistent resolution across all images. Efforts were made to maintain a precise driving trajectory to ensure a constant sensor-to-wall distance throughout the entire tunnel, following reference markers, *e.g.*, lane lines. The camera shutter is triggered by a dedicated synchronization and timing control unit based on OCXO (Oven-Controlled Crystal Oscillator) technology, which ensures high-precision temporal accuracy. Triggering is managed via TTL (Transistor-Transistor Logic) pulses, and all measurement systems are synchronized through a common time base with microsecond-level accuracy. This setup ensures precise temporal alignment across sensors, supporting accurate image stitching and geometric consistency.

The Ground Sampling Distance (GSD), which is the area on the ground covered by a single pixel of the image, was calculated based on acquisition parameters, *i.e.*, focal length of the lens, acquisition speed, and exposure time, and is approximately around 0.0198 mm per pixel. In post-processing, the collected pixel lines were grouped together to form a complete high-resolution image. The images collected of each complete run, thus along the whole tunnel length, were subdivided into blocks of 20 m based on the information given by position sensor. The 20 m-block length was chosen in accordance with the request of Italian regulations for inspections (MIT, 2022a). Due to noise and instability in the odometer data, pixel mapping along the tunnel axis resulted in inaccuracies, *e.g.*, missing pixel lines, when using the native GSD. To ensure spatial consistency and data integrity in the reconstructed images, a conservative pixel step of 0.001 m (corresponding to approximately 1 mm/pixel) was adopted. In the vertical direction, the resolution is defined by the 6144-pixel height of the linear sensor, resulting in a sub-millimetric resolution (typically 0.1 – 0.2 mm/pixel), depending on the camera-to-wall distance. Hence, each image has a dimension of 20000 x 6144 pixels. Additionally, a correction for the optical distortion was applied to the images through general distortion parameters of the used lenses.

4. Results

The proposed methodology was applied for the first time to this exploratory tunnel test case for validating the computed and calculated parameters as well as the extracted coordinates of pixels. The analysis is first discussed on a 20 m section of a polycentric tunnel. The three-dimensional image reconstruction is hereafter presented starting from the actual tunnel cross-section geometry identification through ellipse fitting algorithms. Then, the position and orientation of the acquisition sensor were determined through the optimization process, allowing image pixels mapping into the 3D profile of the infrastructure.

4.1. Ellipse fitting

Six cross-sections along the z-axis were selected from the point cloud of the sample section (20 m length) for best fitting purposes. The primary goal was to determine the geometric parameters of the fitted ellipse for each cross-section and calculate the fitting error. This step allowed evaluating the precision of the fit and the uniformity of the sections and eventual local variations along the selected sector of the tunnel. The main geometric features of the fitted and the respective errors were determined (Table 1): the semi-major (a) and semi-minor (b) axes are relatively consistent across all sections, indicating that the shape of the tunnel remains elliptical throughout the block. Moreover, the a, b values show minimal difference, suggesting an almost circular cross-section for the case at hand. The rotation angle ϕ registers minimal orientation changes along the length of the tunnel, indicating no significant tilt.

To assess the fitting quality of the ellipse to the extracted cross-sections of the tunnel, the radial distances of observed points from the centre were compared with the theoretical radial distances calculated for the fitted ellipse. This error is presented as a percentage for each cross-section and registers low values, indicating an accurate fitting. In general, the geometric parameters and the radial error are consistent across all sections, indicating a good spatial coherence and a regular geometry along the considered range of the point cloud. A slight increase in the radial error is detected in the second and fifth cross-sections, suggesting possible noise in the data. However, the results show consistency with the parameters obtained in the other sections. The representation of the distances between point and ellipse frequency for each

Table 1
Results from the ellipse fitting optimization process: position of the cross-section, semi-major axis (a) and semi-minor axis (b) length, rotation angle of the ellipse (ϕ), and percentage error between radial distances of the point cloud section and the fitted ellipse. In the last column, the mean values for each parameter are reported.

Cross-Section	Position z [m]	a [m]	b [m]	ϕ[rad]	Radial error (%)
1	0.0	5.112	5.162	0.000	0.154
2	3.80	5.122	5.157	−0.001	0.188
3	7.60	5.108	5.183	−0.001	0.186
4	11.40	5.117	5.176	−0.001	0.176
5	15.20	5.112	5.172	0.000	0.191
6	19.00	5.106	5.156	−0.001	0.160
Mean value	–	5.113	5.168	−0.001	–

cross-section is represented in Fig. 7-c, showing a gap lower than 3 cm.

For each cross-section, the coordinates of the ellipse centre (x_0, y_0) were calculated according to the reference system of the point cloud, which is essential to determine the coordinates of the known elements. The representative cross-section for reconstructing the 20 m tunnel segment was determined as the mean value of the overall results of the analysis shown in Table 1. The ellipse fitted to the points of cross-section 4, which present values closer to the mean and is located near the centre of the block (Fig. 7-a), is depicted in Fig. 7-b.

4.2. Orientation and position of the sensor

To calculate the position of the sensor, *e.g.,* the focal point of the lens mounted to the cameras, the genetic algorithm process was applied to reconstruct the 3D model of the 20 m tunnel section for each sector (ceiling and walls). For the model calibration, known reference elements on the tunnel surface were used. Elements on the walls and ceiling were identified both in the image, *i.e.*, pixel position, and in the point cloud, to determine the (x_T, y_T) coordinates corresponding to the cross-sectional geometry of the tunnel. These elements (Fig. 8) were selected within a limited longitudinal extent to maintain geometric consistency, as elements aligned perfectly along the same image row were not always available.

Unknown parameters of the problem, *i.e.*, the sensor position (x_S, y_S) and the starting angle β_0 were defined as decision variables in the optimization procedure, constrained by upper and lower bounds derived from the tunnel cross-section geometry and the physical dimensions of the acquisition system. Results for each tunnel sector are reported in Table 2. The selected hyperparameters (*i.e.*, population size, maximum number of generations) were determined through preliminary trials to balance solution accuracy and computational efficiency. Higher population sizes yielded only small improvements in accuracy at the cost of longer computation times, while lower values led to unstable solutions. The default settings for crossover and mutation functions were retained, as they performed well for the nature of the problem. The final fitness values consistently converged to low residual errors, confirming the robustness of the adopted configuration.

4.3. 3D reconstruction results

The final goal was to reconstruct a 3D model of the tunnel through high-resolution images acquired with a mobile system. This approach enabled the overlap of images from different runs, allowing the reconstruction of the entire tunnel lining. Additionally, the 3D reconstruction

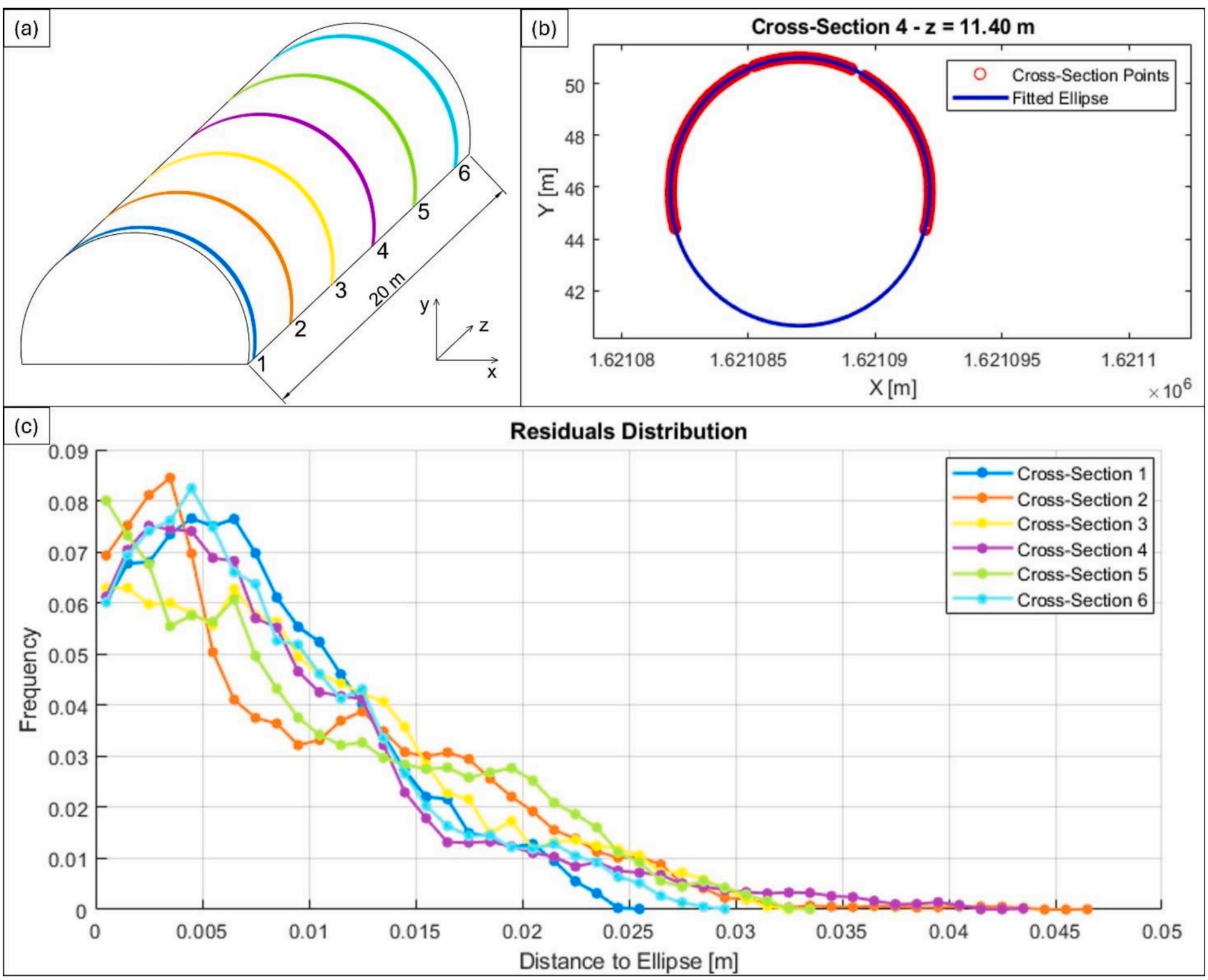

Fig. 7. Ellipse fitting procedure: (a) number of tunnel slices extracted from the point cloud in a range of z-values; (b) representation of the fitted ellipse to the points of Cross-Section (*e.g.*, Section 4); (c) residual distribution for each analysed cross-section showing the frequency of distances from the points to the ellipse.

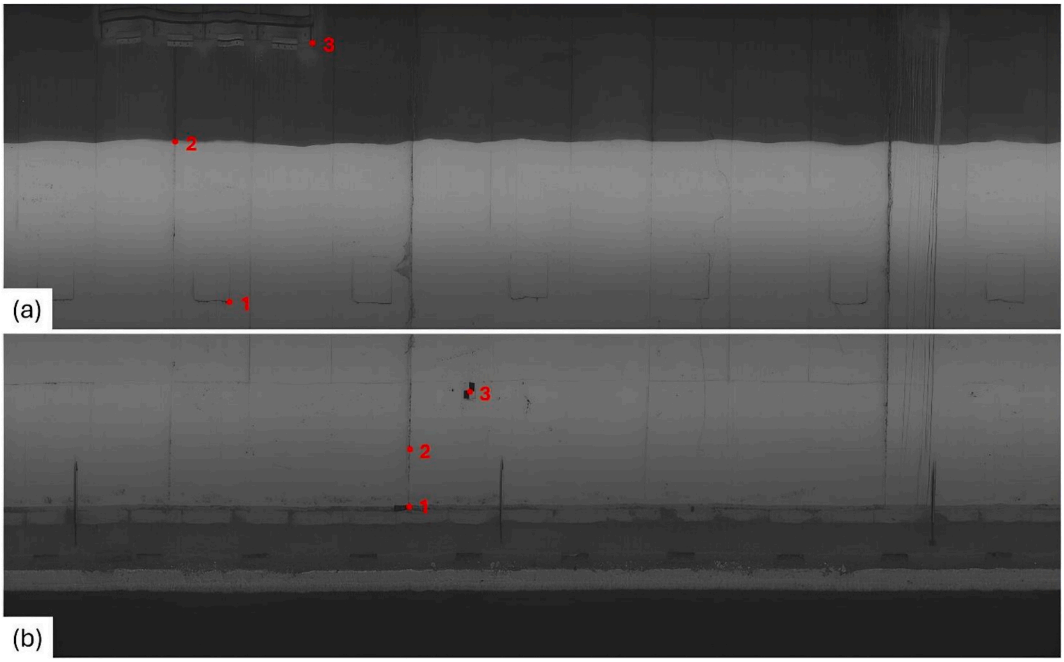

Fig. 8. Position of selected known elements on the tunnel surface to calibrate the genetic algorithm and determine the sensor position, for the left wall images of 20 m length acquired by Cam_01 (a) and Cam_02 (b).

Table 2
Input parameters for the genetic algorithm optimization, *i.e.*, number of target points, population size and maximum number of generations, optimized results of sensor coordinates and angle β_0, and fitness value for each camera (Cam_01 and Cam_02) and tunnel sector: left wall (LW), left ceiling (LC), right ceiling (RC) and right wall (RW).

Tunnel sector	Target points n.	Population Size	Max generations	x_s [m]	y_s [m]	β_0 [°]	Fitness value [m]
Cam_01 – LW	3	800	200	−1.5356	0.9847	127.52	0.0068
Cam_02 – LW	3	800	200	−1.6727	1.2573	186.91	0.0172
Cam_01 – LC	3	800	200	−1.8818	0.5954	34.54	0.0139
Cam_02 – LC	3	800	200	−1.6821	0.5172	89.58	0.0593
Cam_01 – RC	3	800	200	2.0000	0.6803	37.69	0.0200
Cam_02 – RC	3	800	200	2.1116	0.7176	87.99	0.0126
Cam_01 – RW	3	800	200	1.7000	0.9551	−61.99	0.1099
Cam_02 – RW	3	800	200	1.7574	0.5771	0.43	0.0042

provided orthorectified images, ensuring accurate estimation of the actual dimensions of damages and cracks.

A Graphic User Interface (GUI) for the Matlab code was designed in Matlab App Designer to apply the ellipse fitting and to process images captured by each camera (Fig. 9). Once the sensor parameters were determined, it was possible to calculate 2D coordinates (x, y) for each pixel of the image. For each 20 m length image of the tunnel walls and ceilings captured by *Cam_01* and *Cam_02*, the calculated (x, y) coordinates were plotted (S1 and S2 in Supplementary Material). 20 m-image blocks from each run were processed, where (x, y, z) coordinates were assigned to each pixel. The result is a 3D point cloud containing both coordinates and intensity information. For consistency in representation and comparison with the original 3D point cloud in Cloud Compare software (Girardeau-Montaut, 2024), the (x, y) axes were transformed into (x, z), and the axis representing the tunnel direction was assigned to y. Giving the known length of the image, the y coordinates were determined by distributing the pixels along a 20 m section. To reconstruct the final 3D model of the surface of the tunnel, point clouds generated from each image (S3 in Supplementary Material) were stitched together, cutting the overlapping zones from the point cloud (Fig. 10).

To verify the variations in distance given by the ellipse fitting method, a comparison was made between the point cloud acquired by the mobile mapping system and the point cloud generated by the proposed tool. This comparison was performed using the *Cloud-to-Cloud* (C2C) distance function (Girardeau-Montaut et al., 2005) in Cloud Compare. The MLS point cloud was selected as the reference for computing the distances between the datasets. The absolute distances vary primarily on the left side of the wall (Fig. 11), but with distance values generally not exceeding 3 cm, as reported for the ellipse fitting results (Fig. 7). To further assess the reliability of the reconstruction, a second comparison was performed using the *Multiscale Model-to-Model Cloud Comparison* (M3C2) function in Cloud Compare (Lague et al., 2013). Unlike the C2C method, which measures direct Euclidean distances between nearest points, the M3C2 approach calculates distances along the surface normal, considering local surface geometry and scale. This results in a more robust and reliable measure of change, particularly for rough, irregular, or curved surfaces like tunnels. The M3C2 analysis confirms the overall similarity between the two models: values range from –6 cm to 6 cm, although most deviations generally do not exceed ± 3 cm (Fig. 12a). The distance distribution (Fig. 12b) is centred around zero, with the main Gaussian component (D1) exhibiting a standard deviation of approximately 0.014 m. Minor deviations, represented by the lateral components D2 ($\mu = -0.037$ m, $\sigma = 0.011$ m) and D3 ($\mu = 0.039$ m, $\sigma = 0.014$ m), can reasonably be attributed to local variations in surface roughness, construction irregularities, and minor misalignments between the point clouds. These differences may also stem from minor changes in local orientation or slope within the

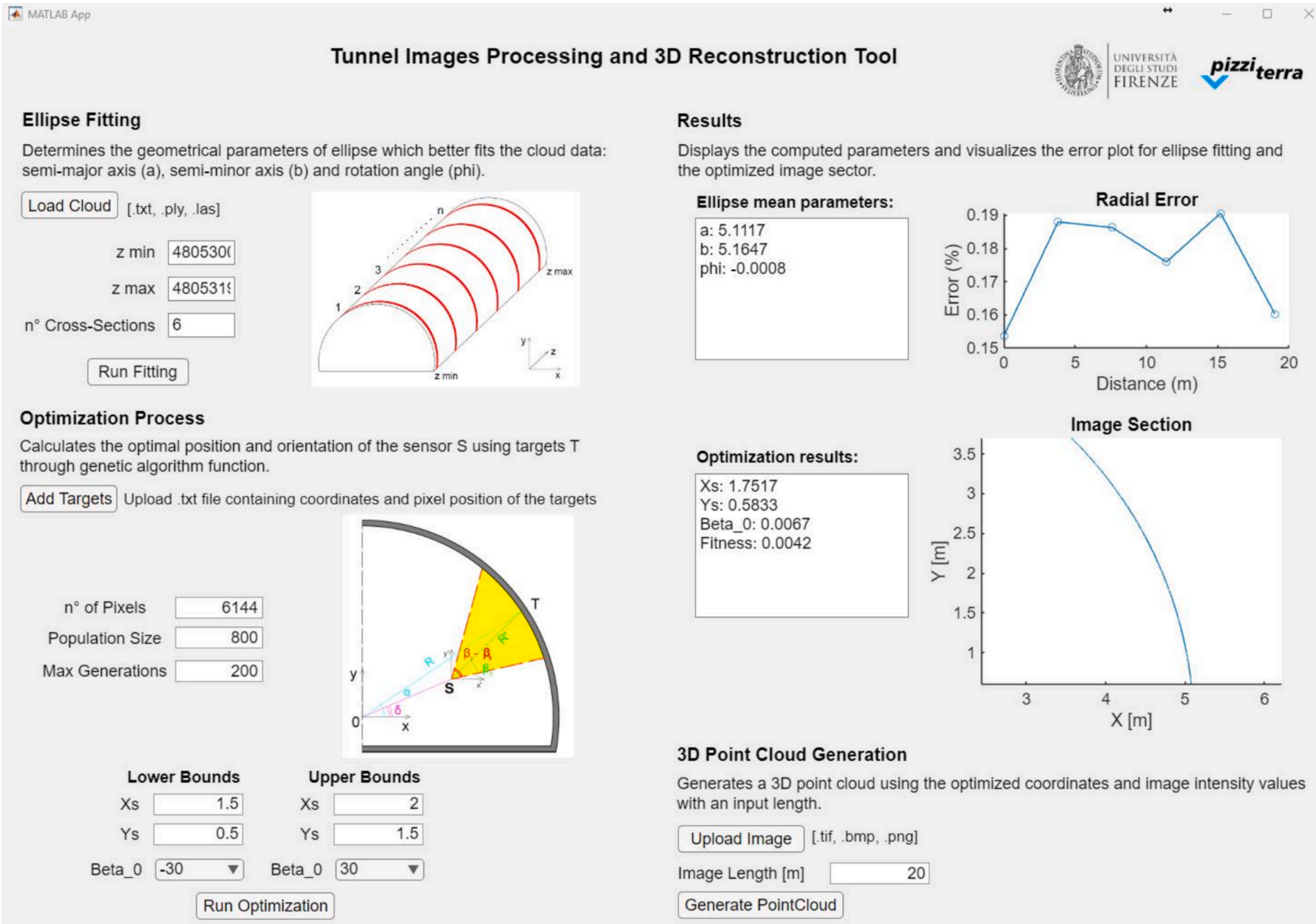

Fig. 9. Graphic User Interface (GUI) developed on Matlab for the 3D image reconstruction procedure described in this paper.

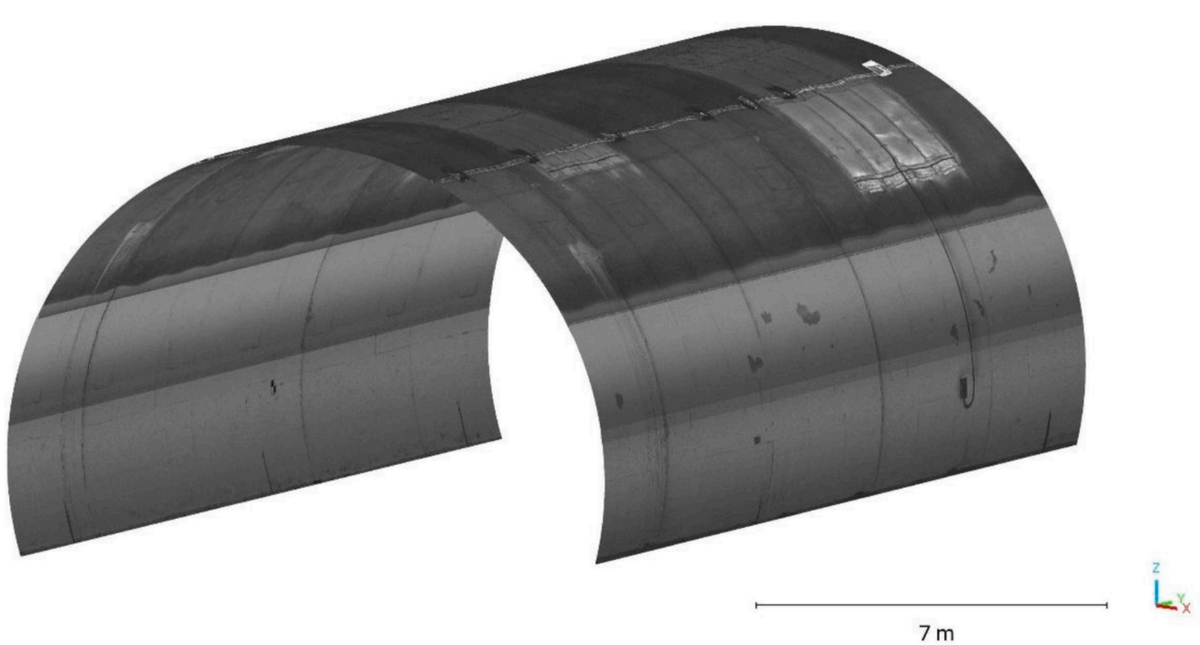

Fig. 10. 3D point cloud of the tunnel obtained by the tool.

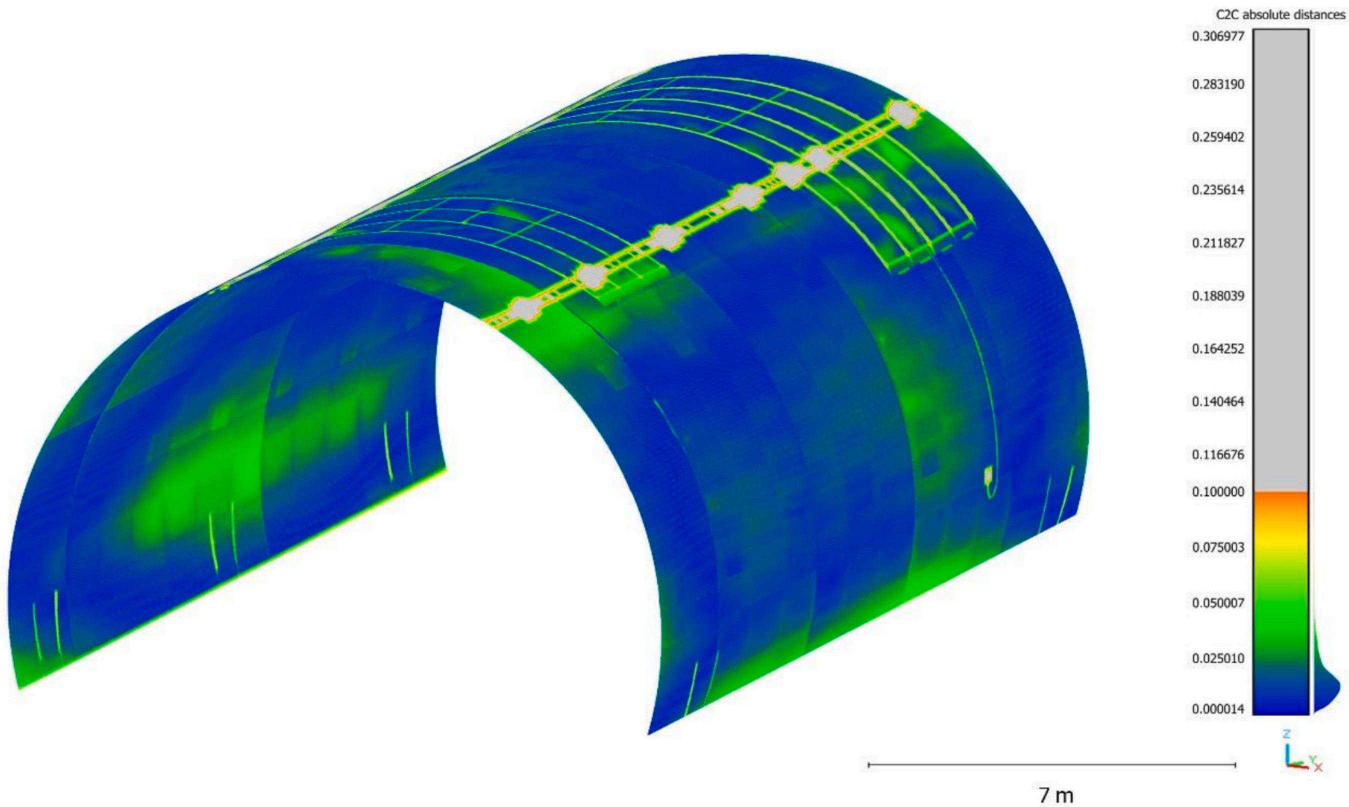

Fig. 11. Representation of distance variation between the point cloud by LiDAR scan and point cloud generated by the tool with C2C algorithm.

reconstructed model. In addition to these physical factors, small discrepancies may also result from the geometric simplification introduced by the ellipse fitting process, which may introduce local inaccuracies in more complex or asymmetric geometries. Overall, both methods consistently confirm that the ellipse-based reconstruction closely matches the reference geometry: the C2C method provides an overview of general alignment, while the M3C2 method offers a more robust and surface-aware validation of geometric accuracy.

Finally, results of the ellipse fitting procedure are presented for all n° 17 tunnel segments (20 m each) to assess the geometric continuity along the entire alignment. For each block, the mean values of the semi-major and semi-minor axes were calculated from six cross-sections, and the differences across consecutive block boundaries were analysed. The results show limited variability, with median differences of $|\Delta a| = 0.0092$ m (25th percentile = 0.0034 m, 75th percentile = 0.0163 m) and $|\Delta b| = 0.0026$ m (25th percentile = 0.0013 m, 75th percentile = 0.0048 m). The section-level distribution of all cross-sections (Fig. 13) across the tunnel (17 × 6 values) further confirms that no significant discontinuities are present, with variations confined to the centimetric range. Interestingly, the statistical distribution indicates that the semi-major axis a exhibits greater variability than the semi-minor axis b (Fig. 13). This difference may be related to small construction irregularities or to minor deviations in the tunnel geometry accumulated along its length. Additional details on the analysis, including block-by-block boxplots and boundary-wise differences, are provided in the Supplementary Material (S4 and Table S1).

Texture continuity across adjacent blocks was verified. Orthophotos of two consecutive blocks (S5 in Supplementary Material) show that surface features are preserved at the stitching boundaries. Small local mismatches can occur due to factors such as slight trajectory deviations, pavement irregularities or vibrations during acquisition. However, these effects are limited to very small areas and do not influence the overall result.

5. Discussion

In Italy, current regulations for tunnel inspections typically require LiDAR scans as a standard practice. While 3D point cloud data provides valuable information for capturing tunnel geometry, it often limits visibility to larger defects, easily detectable due to the lower resolution of the scans. In this context, the addition of high-resolution photographic surveys has provided a detailed representation of the actual tunnel surface. Images enable the detection of smaller-scale defects that would not be visible through LiDAR technologies alone, significantly enhancing the accuracy and detail of structural evaluations.

Even though the inspection practice requires a visual inspection of the tunnel conducted on-site, the proposed methodology and mobile image survey can be used as a preliminary analysis: the high-resolution images recorded with the *TunnelEye* system can provide useful information on most critical sectors. Moreover, pictures represent a graphic support for defect recognition and classification. The image repository can greatly enhance the back-office work. A 3D reconstruction of the images is automatically performed to ensure correct scaling as a first processing step. In conventional workflows, cracks are usually detected directly on 2D images and subsequently projected into 3D space. This process may introduce geometric uncertainty and potentially require additional post-processing. By contrast, the proposed method first performs a 3D reconstruction to geometrically correct high-resolution images, so that each pixel is expressed in metric coordinates. This allows defect detection to be carried out in a scaled and georeferenced domain, ensuring direct accurate measurements. Such integration enhances the engineering relevance of the inspection on orthophoto obtained from a 3D model, enabling both reliable defect quantification and a more informed structural interpretation.

Compared to conventional SfM and photogrammetry-based approaches, the proposed method demonstrates several practical advantages. Traditional photogrammetric reconstructions require overlapping images captured from multiple angles and are highly dependent on

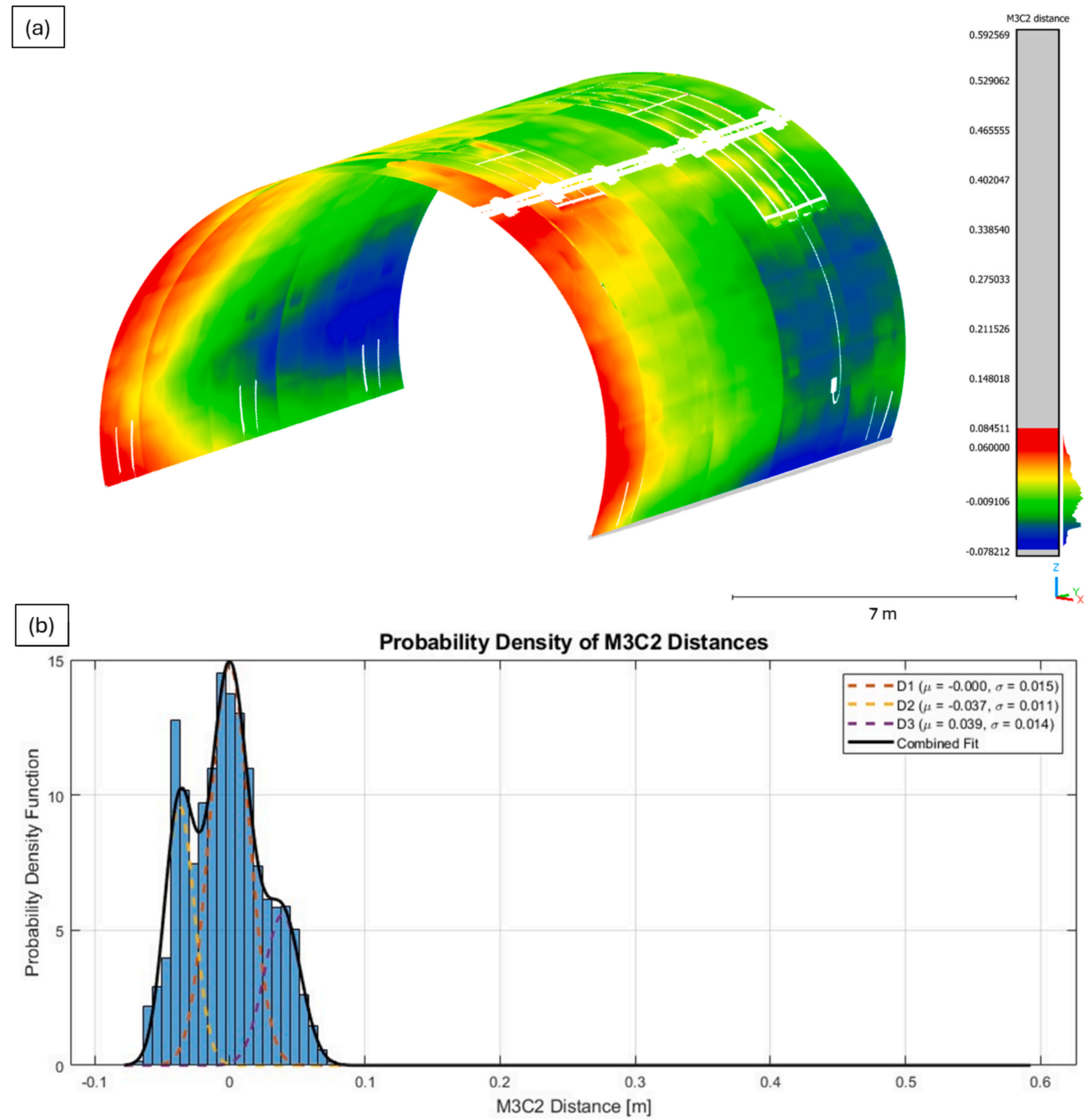

Fig. 12. Representation of spatial deviations between the LiDAR-derived point cloud and the ellipse-fitting-based reconstruction, computed by the M3C2 algorithm. (a) M3C2 distance map highlighting spatial deviations across the tunnel surface; (b) probability density of M3C2 distances.

consistent lighting and texture-rich surfaces, which are difficult to obtain in tunnel environments. In contrast, the proposed method enables 3D reconstruction from linear, high-resolution image strips acquired under controlled lighting conditions using a mobile platform. This overcomes the limitations of perspective-based matching inherent in SfM, which proved ineffective in our trials.

The primary challenge of the proposed method involves determining the exact position and orientation of the sensor during data acquisition, which is critical for accurately estimating the acquisition area of both cameras. In this approach it was necessary to reconstruct a geometric model of the tunnel cross-section to calculate its position and orientation, using known point coordinates obtained from a separately conducted laser scanning survey. These target elements needed to be identifiable both in the images and in the point cloud and were selected to be evenly distributed and homogeneously placed within the image. However, for some images it was not possible to select optimal targets, *e.g.*, the lower portion of wall images captures parts of the sidewalk and asphalt, which are not relevant for reconstructing the elliptical surface of the tunnel. As shown in Table 2, the right wall image captured by *Cam_01* presents a higher fitness value. This can be attributed to the targets which are located in a specific area of the image (this also applies to the left wall image presented in Fig. 8-b), making it more challenging

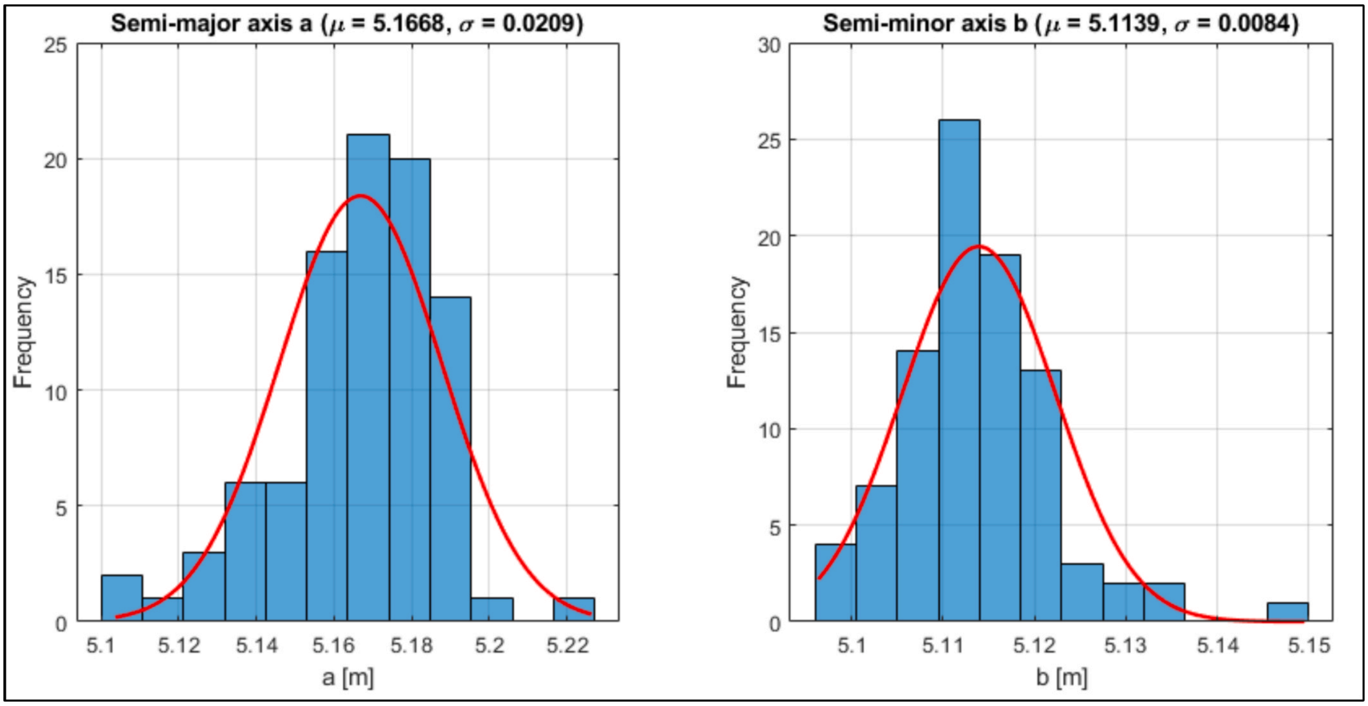

Fig. 13. Statistical distribution of the frequency of the semi-major axis a (left) and semi-minor axis b (right), with overlaid Gaussian fits (red curve), across all tunnel cross-sections (17 blocks × 6 sections). (For interpretation of the references to colour in this figure legend, the reader is referred to the web version of this article.)

for the genetic algorithm to converge to the minimum fitness value and, consequently, to a solution that can be considered acceptable and realistic. The same problem arose for the ceiling images which capture the farthest extremes from the sensor. These areas appear darker, making it more difficult to identify and select targets. In this first case study, the number of targets was kept to the minimum required for a reliable

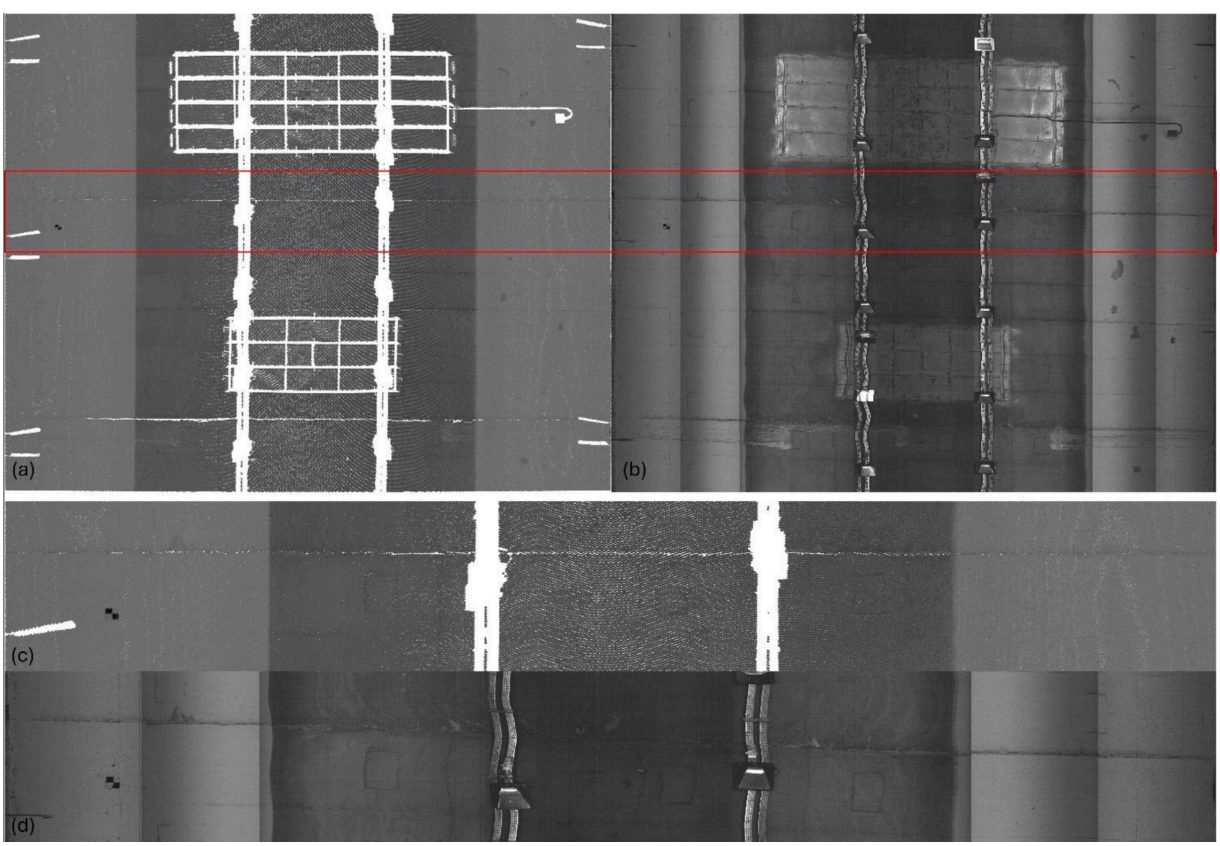

Fig. 14. Comparison between orthophotos extracted from high-resolution images 3D reconstruction (a) and mobile laser scanner point cloud (b), with the respective zoomed-in views (c) and (d).

reconstruction, in line with practical inspection constraints where target deployment must be reduced to limit interference with traffic and to operate safely. While a higher number of targets with balanced spatial distribution would generally improve the accuracy of the fitting, the adopted configuration reflects realistic operational conditions under which the proposed method is expected to be applied. The sensitivity of the method to this parameter will be deeper investigated in future work using datasets with a greater number of suitable target points. Despite these issues, it was possible to obtain optimal solutions which generated 3D point clouds of the images. In Fig. 14, a comparison between the image obtained from point cloud unrolling and the image from acquired high-resolution images is shown: the match between the two, in terms of position and scaling, is very satisfactory and appropriate for defect assessment classification purposes.

Another important issue concerns the metrics for defect detection. In the acquired images, a reference target (20 × 20 cm) was placed alongside with a thickness gauge consisting of black bars with widths ranging from 0.1 to 5 mm (Fig. 15). These reference elements enabled an independent validation of the dimensional accuracy of the reconstructed point cloud. The dimensional check on the square target confirmed the global scaling of the reconstruction, with deviations within the millimetric range. A small discrepancy between the reconstructed width (–0.9 mm) and height (+5.8 mm) of the square target was observed. This may be attributed to geometric distortions related to trajectory deviations during data collection. Measurements on the thickness gauge further highlighted the effective resolution of the system: thicknesses $\geq$ 1.6 mm were consistently reproduced with sub-millimetric accuracy (errors $\leq$ 0.1–0.3 mm), whereas thinner elements were captured but not clearly distinguishable for measurement. This threshold reflects the resolution of the input images and the natural point dispersion inherent to the reconstruction process. Such analysis provided a practical indication of the smallest defect size that can be reliably detected in real inspection scenarios. Hence, the practical relevance for engineering tasks such as crack measurement and millimetric defect classification is effectively demonstrated.

Given the high resolution of the images, the processing of a 20 m length block, representing the whole tunnel vault, takes approximately 15 min with an *Intel® Core™ i9* PC. Processing time is significantly lower than photogrammetric approaches and does not require complex camera calibration. The resulting point cloud for the single images is composed of 122′880′000 points, and its density is determined by the resolution of the processed images. To optimize the processing time, the resolution can be reduced by subsampling the final point cloud, balancing it with the desired resolution. The choice of a 20 m segmentation length is indeed consistent with Italian inspection regulations, which prescribe defect assessment over comparable spans, and represents a practical balance between computational efficiency and geometric reliability.

Additionally, best fitting methods to determine the tunnel geometry proved to be adequate for representing the real model of the tunnel as accurately as possible (Weixing et al., 2020), and the fitting with an ellipsoidal shape was suitable and effective for representing this specific case study. The employment of the *fminsearch* function to calculate the minimum ellipse fitting error has proved to be adequate to the point cloud data used for this work, allowing more flexibility and robustness in case of noise and outliers. This function converges to the optimal solution with lower computational time compared to more complex optimization algorithms, *e.g.*, genetic algorithms (Walton et al., 2014). In the presented case study, the cross-section is nearly circular. Therefore, an elliptical approximation provides a reliable geometric representation with negligible impact on accuracy. To verify the applicability of the ellipse-fitting method to more asymmetric tunnel profiles, a cross-section from a different tunnel was analysed. In this case, the fitted ellipse had a semi-major axis of 6.729 m and a semi-minor axis of 6.451 m, with a radial error of approximately 0.25 %. Although this geometry deviates more from circular symmetry, the results remain within an acceptable error margin, as shown in the residual distribution (see Fig. 16). This suggests that the method is well-suited for tunnels that are almost elliptical and regular in shape, though the fitting error increases as the shape deviates from circularity. For more complex or asymmetric shapes (*e.g.*, horseshoe, egg-shaped profiles), or for local geometric variations along the tunnel alignment (*e.g.*, lay-bys, widened zones), further adaptation of the geometric equations is necessary. To overcome this limitation, ongoing development involves integrating a LiDAR sensor into the acquisition system: this will allow for direct acquisition of the tunnel geometry, enabling accurate reconstruction of complex cross-sectional shapes and improving the overall reliability of the method. Despite this, the proposed approach offers a robust and computationally efficient solution for the 3D reconstruction of tunnel profiles in many real-world applications. As already mentioned, direct use of LiDAR data allows for geometric modelling, but lacks the resolution required for detecting small-scale defects. The proposed approach, based on ellipse fitting and genetic optimization, addresses this limitation by achieving sub-centimetric alignment between images and the tunnel geometry. This is evidenced by: *(i)* the main Gaussian

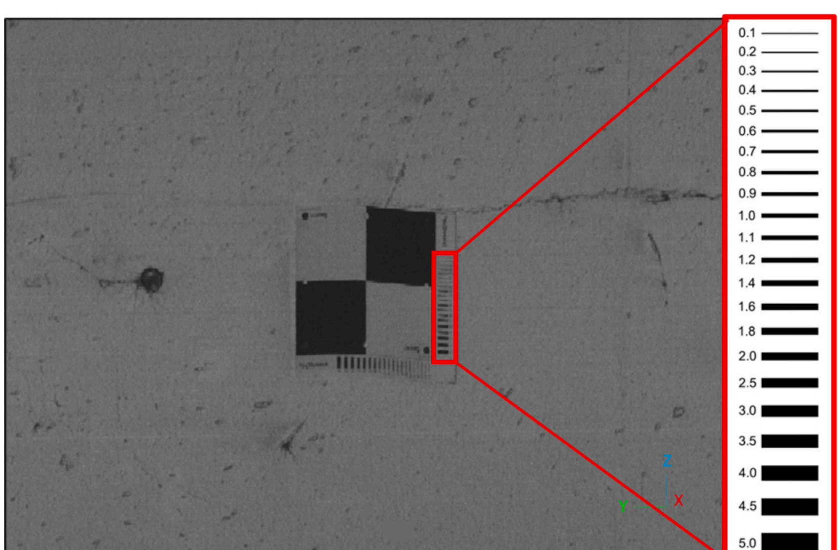

Fig. 15. Zoom on the reference calibration setup, including a 20 × 20 cm square target and thickness gauges composed of black bars with widths ranging from 0.1 to 5 mm.

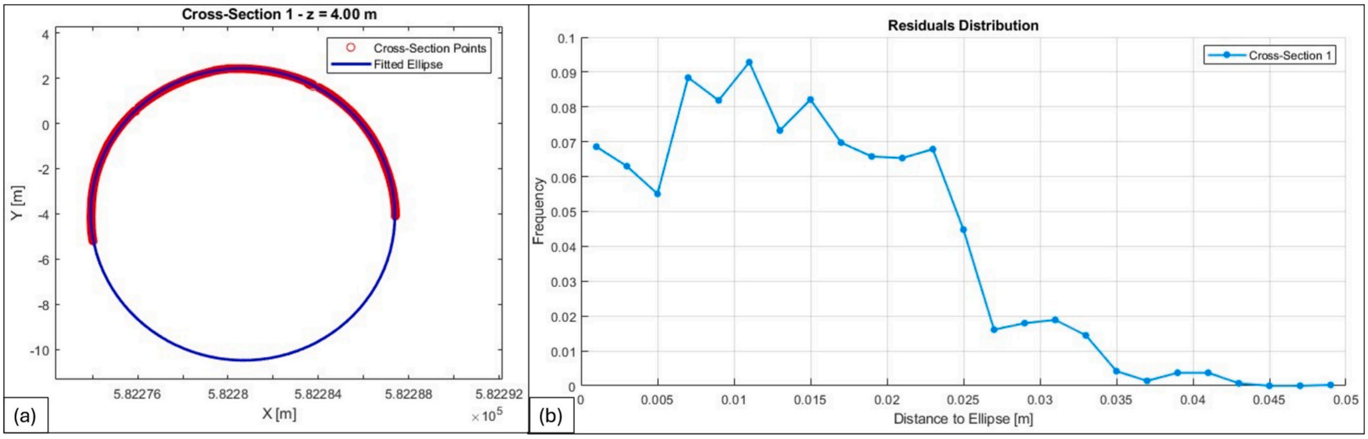

Fig. 16. Example of geometric approximation of a tunnel cross-section using ellipse fitting, performed on a second case study. (a) Best-fit ellipse overlaid on the extracted points of the cross-section; (b) Residual error distribution indicating the deviation of the original points from the fitted ellipse.

distribution of M3C2 distances ($\mu \approx 0$, $\sigma \approx 0.015$ m), indicating strong consistency between the reconstructed and reference point clouds, and *(ii)* the accurate pixel-to-coordinate mapping. Both the C2C and M3C2 analyses show that deviations between models are mostly within $\pm$ 3 cm. This is an acceptable error and comparable to the typical accuracy of mobile LiDAR systems in tunnels. It is worth noting that the proposed method does not aim to exceed LiDAR in geometric precision, but to complement it by adding high-resolution texture data. This integration enhances tunnel inspection workflows by combining reliable geometric reconstruction with detailed surface information.

Another important point of current development is the use of the trajectory data provided by inertial sensors to aid in 3D reconstruction. This data allows the recreation of the tunnel trajectory curvature, providing a more realistic 3D model of the tunnel geometry. By integrating the precise movement of the sensor, the resulting model will help simulate realistic alignment and curvature, and correct distortion caused by vibration and warp effects with pitch and roll angles measured by Inertial Measurement Unit (IMU).

The proposed method of 3D image reconstruction can also be adapted for different types of images, *e.g.*, thermal images. Integrating thermal imaging would be particularly advantageous for assessing temperature anomalies, which could indicate water infiltration or areas with different thermal properties. Knowing the tunnel cross-sectional geometry, the method can be applied to a variety of imaging technologies. One of the long-term goals of this project is indeed to compare and integrate various datasets obtained from multiple types of instruments. This includes combining data from radar technologies, georadar, thermal cameras, deformation maps, as well as information from traditional monitoring tools, large-scale susceptibility studies, and public databases. By compiling data from diverse sources, the proposed system could provide a holistic view of tunnel conditions, enhancing the reliability and robustness of the inspection process. Maintenance procedures would also benefit from a comprehensive information hub, and this is believed to be an important development in digitalization of asset management procedures. Temporal analysis is another area of application, allowing for the comparison of datasets acquired at different points in time. This type of analysis is critical for understanding how the structural condition of the tunnel evolves, detecting emerging problems, and tracking changes over time. In this framework, another future development of the system is the combination of real-time monitoring technologies (Broere, 2024). The 3D reconstructed environment can be used with data from sensors, *e.g.*, strain gauges, displacement sensors. This would allow continuous monitoring of tunnel conditions under normal use and enable real-time tracking of structural deformations and crack propagation, thereby providing early warnings and improving safety. By linking sensor data with high-resolution image models, the system could support faster and more accurate maintenance decisions.

Lastly, the methodology was applied to represent cracks detected from high-resolution images in a three-dimensional environment. Once determined the position of a certain number of pixels along the crack within the image, it was possible to create points with (x, y, z) coordinates representing the crack pattern thanks to the previous 3D mapping of the pixels in the full image. Finally, a polyline was reconstructed from the generated points, allowing to measure and visualize the crack in a 3D space (Fig. 17). Specific techniques can be developed to automatically detect and filter crack elements on images; for instance, AI algorithms and Digital Image Correlation (DIC) techniques for crack detection and measurement have already been successfully tested on 2D images (Foria et al., 2022; Belloni et al., 2023; Li et al., 2024; Xu et al., 2024; Lu et al., 2025). As part of the *TunnelEye* project, an AI algorithm was developed and demonstrated the ability to locate 0.5 mm cracks on high-resolution 2D images. The integration of such AI techniques with the proposed 3D reconstruction model is currently being explored and implemented as part of ongoing research activities, enabling not only automated detection and classification but also predictive insights based on spatial distribution and morphological patterns of detected anomalies. This could further improve the efficiency and accuracy of tunnel inspection and long-term monitoring activities. As a final step, all the information regarding monitoring, survey and defects analysis can potentially be integrated into a three-dimensional, georeferenced management and maintenance hub. Since damage and deformations are frequently influenced by geological and geotechnical conditions, a comprehensive representation of all elements playing a role in the tunnel safety assessment is essential to support integrated data management and safety assessment of the tunnel.

6. Conclusions

The paper presents an automatic calculation algorithm providing the three-dimensional reconstruction of tunnel infrastructure using 2D high-resolution images. The study is based on the availability of high-quality pictures acquired with an innovative mobile technology (*TunnelEye*) that allows capturing images of the tunnel lining using a vehicle equipped to drive along the infrastructure. The methodology consists of positioning in 3D each pixel of the acquired image based on the geometric model of the acquisition scheme. This was accomplished by implementing a Matlab routine to solve an unconstrained optimization problem. The tool was applied to a 20 m tunnel test case, where laser scanner survey and high-resolution image survey were performed in the framework of periodic inspection.

The study proved the good performance of the theoretical geometric model: the geometry of the tunnel section was first described using an

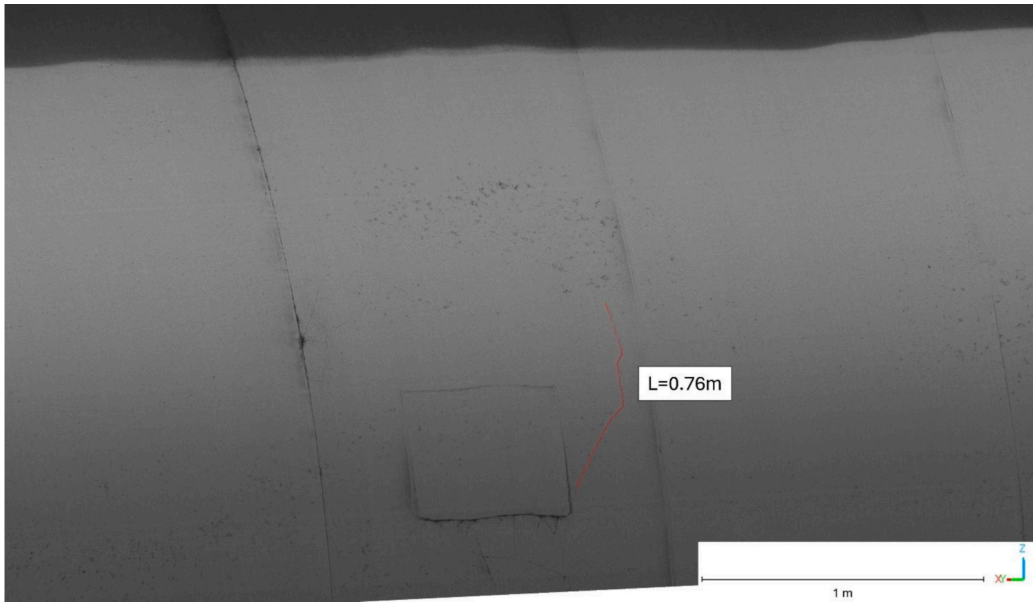

Fig. 17. 3D crack polyline highlighted in red in the point cloud. The measured length of the polyline is 0.76 m and the measured thickness of the crack is 1.2 mm ± 0.3 mm. (For interpretation of the references to colour in this figure legend, the reader is referred to the web version of this article.)

ellipse equation to which 3D coordinates were assigned for each image pixel. Target points detectable both in the georeferenced point cloud and in the images were used for calibration purposes. The 3D reconstruction provided the best representation and visualization of the elements inside the tunnel. The major advantage of the tool is the possibility of identifying and evaluating structural defects and cracks in the tunnel surface directly on a scaled model, with the possibility to evaluate their length and impact.

Mobile image survey can be used as a preliminary analysis in the tunnel inspection process: the high-resolution images can provide useful information on the most critical sectors. Moreover, they represent a graphic support for defect recognition and classification. The image repository can greatly enhance back-office work.

This work can help in advanced assessment analyses, providing an enhanced representation and a better understanding of the effects on infrastructure within its geological context. If subsequent surveys are conducted, the comparison of 3D models can also provide monitoring of defects and deformation over time.

CRediT authorship contribution statement

Saduni Melissa Dahanayaka: Writing – original draft, Investigation, Formal analysis, Data curation. **Adrian Riquelme Guill:** Writing – review & editing, Supervision, Methodology, Conceptualization. **Alessia Vecchietti:** Writing – review & editing, Validation, Supervision, Project administration. **Matteo Del Soldato:** Writing – review & editing, Supervision, Project administration, Funding acquisition.

Declaration of competing interest

The authors declare that they have no known competing financial interests or personal relationships that could have appeared to influence the work reported in this paper.

Acknowledgements

This research was conducted under the PNRR doctoral program on innovation and collaboration with industry (Mission 4, Component 2, Investment 3.3, Ministerial Decree 352/2022). *TunnelEye* hardware system has been developed conjunctively by pizzi terra S.r.l. and terra vermessungen ag. Suggestion from Dr. S. Derler, Dr. S. Häberling and Eng. S. Shütz of terra vermessungen ag and support from the staff of pizzi terra S.r.l. are gratefully acknowledged.

Appendix A. Supplementary data

Supplementary data to this article can be found online at https://doi.org/10.1016/j.tust.2025.107181.

Data availability

Data will be made available on request.

References

Attard, L., Debono, C.J., Valentino, G., Di Castro, M., 2018. Tunnel inspection using photogrammetric techniques and image processing: A review. ISPRS J. Photogramm. Remote Sens. 144, 180–188. https://doi.org/10.1016/j.isprsjprs.2018.07.010.

Barla, M., Barbero, M., Baralis, M., Insana, A., Milan, L., Rosso, E., Selleri, A., Marchiondelli, A., Mele, P., Tripoli, L., Zilli, L., 2021. A method to define the priority for maintenance and repair works of Italian motorway tunnels. IOP Conf. Ser.: Earth Environ. Sci 833 (1), 012175. https://doi.org/10.1088/1755-1315/833/1/012175.

Belloni, V., Sjölander, A., Ravanelli, R., Crespi, M., Nascetti, A., 2023. Crack monitoring from Motion (CMfM): Crack detection and measurement using cameras with non-fixed positions. Autom. Constr. 156, 105072. https://doi.org/10.1016/j.autcon.2023.105072.

Beltrami, C., Bianchi, S., Cervio, M., Anghileri, M., Felicetti, R., Quattrone, A., Masala, D., 2021. Bridge visual inspections: Experience of local authorities and the case study of the Corso Grosseto viaduct. In: Bridge Maintenance, Safety, Management, Life-Cycle Sustainability and Innovations. CRC Press, pp. 3358–3364.

Broere, W., 2024. Smart monitoring of tunnels. In Geotechnical Aspects of Underground Construction in Soft Ground. CRC Press, pp. 19–29.

Brownjohn, J.M.W., 2007. Structural health monitoring of civil infrastructure. Philos. Trans. R. Soc. A Math. Phys. Eng. Sci. 365 (1851), 589–622. https://doi.org/10.1098/rsta.2006.1925.

Buggiani, D., Malavisi, M., Baldacci, A., 2024. Digital technologies for bridge damage detection: Drones and AI for remote inspections. In: Bridge Maintenance, Safety, Management, Digitalization and Sustainability. CRC Press, pp. 3161–3168.

Cereyon, A., Weber, W., Wissler, R., Wittwer, A., 2019. Advanced 4-channel scan system for tunnel inspection. In: Tunnels and Underground Cities. Engineering and Innovation Meet Archaeology, Architecture and Art. CRC Press, pp. 1906–1916.

Chaiyasarn, K., Kim, T.-K., Viola, F., Cipolla, R., Soga, K., 2016. Distortion-free image mosaicing for tunnel inspection based on robust cylindrical surface estimation through structure from motion. J. Comput. Civ. Eng. 30 (3), 04015045. https://doi.org/10.1061/(ASCE)CP.1943-5487.0000516.

Chen, S., Laefer, D.F., Mangina, E., Zolanvari, S.M.I., Byrne, J., 2019. UAV bridge inspection through evaluated 3D reconstructions. J. Bridg. Eng. 24 (4), 05019001. https://doi.org/10.1061/(ASCE)BE.1943-5592.0001343.

Ding, X., Chen, S., Duan, M., Shan, J., Liu, C., Hu, C., 2024. Towards 3D reconstruction of multi-shaped tunnels utilizing mobile laser scanning data. Remote Sens. (Basel) 16 (22), 4329. https://doi.org/10.3390/rs16224329.

Doreau-Malioche, J., Paillette, F., Puglia, M., Spohn, P., Frachon, S., Poli, B., 2023. In: Tunnel Inspections with the Aid of High-Performance Image Acquisition Tools: an Insight on Key Parameters for a Successful Detection of Structural Defects. CRC Press, pp. 3048–3056. https://doi.org/10.1201/9781003348030-368.

European Commission, 2022. RIMA – Robotics for Infrastructure Inspection and Maintenance (Grant Agreement No. 824990, 2021–2022) [Project]. Horizon 2020 Programme.

Farahani, B.V., Barros, F., Sousa, P.J., Cacciari, P.P., Tavares, P.J., Futai, M.M., Moreira, P., 2019. A coupled 3D laser scanning and digital image correlation system for geometry acquisition and deformation monitoring of a railway tunnel. Tunn. Undergr. Space Technol. 91, 102995. https://doi.org/10.1016/j.tust.2019.102995.

Foria, F., Avancini, G., Ferraro, R., Miceli, G., & Peticchia, E. (2019). ARCHITA: an innovative multidimensional mobile mapping system for tunnels and infrastructures. In MATEC Web of Conferences (Vol. 295, p. 01005). EDP Sciences. Doi: 10.1051/matecconf/201929501005.

Foria, F., Miceli, G., Calicchio, M., Catigbac, G.M., Loprencipe, G., 2022. In: Digital Transformation in the Visual Inspection of Heritage Railways Tunnels: Technology, Artificial Intelligence and Methodology. CRC Press, pp. 337–348. https://doi.org/10.1201/9781003308867-20.

Foria, F., Calicchio, M., Moretti, L., Loprencipe, G., 2023. Multidimensional mobile mapping and integrated approach for the digitalisation of underground transport infrastructure. Acta Polytechnica 63 (2), 111–122. https://doi.org/10.14311/AP.2023.63.0111.

Gaspari, F., Barbieri, F., Duque, J.P., Fascia, R., Ioli, F., Zani, G., Pinto, L., 2023. a Geo-database for 3D-AIDED multi-epoch documentation of bridge inspections. Int. Arch. Photogram., Remote Sens. Spatial Inform. Sci. 48, 299–306. https://doi.org/10.5194/isprs-archives-XLVIII-1-W2-2023-299-2023.

Gavilán, M., Sánchez, F., Ramos, J. A., & Marcos, O. (2013, December). Mobile inspection system for high-resolution assessment of tunnels. In The 6th International Conference on Structural Health Monitoring of Intelligent Infrastructure (p. 10).

Girardeau-Montaut, D., 2024. Cloud Compare: 3D point cloud and mesh processing software, open-source project. Online: http://www.danielgm.net Version 2.13.2).

Girardeau-Montaut, D., Roux, M., Marc, R., Thibault, G., 2005. Change detection on points cloud data acquired with a ground laser scanner. Int. Arch. Photogram., Remote Sens. Spatial Inform. Sci. 36 (3), W19.

Golberg, D.E., 1989. Genetic algorithms in search, optimization, and machine learning. Addion Wesley. Reading 673, 3.

Huang, H., Sun, Y., Xue, Y., Wang, F., 2017. Inspection equipment study for subway tunnel defects by grey-scale image processing. Adv. Eng. Inf. 32, 188–201. https://doi.org/10.1016/j.aei.2017.03.003.

Iacobini, F., Pranno, A., 2023. Mobile mapping systems and algorithms for Italian tunnel assessment. In: Expanding Underground-Knowledge and Passion to Make a Positive Impact on the World. CRC Press, pp. 2431–2436. https://doi.org/10.1201/9781003348030-292.

Lagarias, J.C., Reeds, J.A., Wright, M.H., Wright, P.E., 1998. Convergence properties of the Nelder-Mead simplex method in low dimensions. SIAM J. Optim. 9 (1), 112–147. https://doi.org/10.1137/S1052623496303470.

Lague, D., Brodu, N., Leroux, J., 2013. Accurate 3D comparison of complex topography with terrestrial laser scanner: Application to the Rangitikei canyon (NZ). ISPRS J. Photogramm. Remote Sens. 82, 10–26. https://doi.org/10.1016/j.isprsjprs.2013.04.009.

Liao, J., Yue, Y., Zhang, D., Tu, W., Cao, R., Zou, Q., Li, Q., 2022. Automatic tunnel crack inspection using an efficient mobile imaging module and a lightweight CNN. IEEE Trans. Intell. Transp. Syst. 23 (9), 15190–15203. https://doi.org/10.1109/TITS.2021.3138428.

Li, D., Cheng, B., Shi, L., Xiang, S., Zhao, Q., 2024. An automated measurement method for the fatigue crack propagation based on decorrelated digital image correlation. Int. J. Fatigue 183, 108265. https://doi.org/10.1016/j.ijfatigue.2024.108265.

Lu, G., Kou, L., Yan, W., Niu, P., Liu, J., 2025. MB-YOLO: a deep learning-based network for detecting cracks in highway tunnel linings. Meas. Sci. Technol. 36 (6), 065405. https://doi.org/10.1088/1361-6501/addbfd.

Machado, L.B., Futai, M.M., 2024. Tunnel performance prediction through degradation inspection and digital twin construction. Tunn. Undergr. Space Technol. 144, 105544. https://doi.org/10.1016/j.tust.2023.105544.

Mahmoodian, M., Shahrivar, F., Setunge, S., Mazaheri, S., 2022. Development of digital twin for intelligent maintenance of civil infrastructure. Sustainability 14 (14), 8664. https://doi.org/10.3390/su14148664.

Mandirola, M., Casarotti, C., Peloso, S., Lanese, I., Brunesi, E., Senaldi, I., 2022. Use of UAS for damage inspection and assessment of bridge infrastructures. Int. J. Disaster Risk Reduct. 72, 102824. https://doi.org/10.1016/j.ijdrr.2022.102824.

Ministero delle Infrastrutture e dei Trasporti (MIT) – Consiglio Superiore dei Lavori Pubblici. (2022). Linee guida per la classificazione e gestione del rischio, la valutazione della sicurezza ed il monitoraggio delle gallerie esistenti. Rome, Italy. https://cslp.mit.gov.it/sites/default/files/ALL%20DM%20247%20Allegato_1_-_LL_GG_gallerie_con_allegati_A-B-C1-C2-D.pdf.

Ministero delle Infrastrutture e dei Trasporti (MIT) – Consiglio Superiore dei Lavori Pubblici. (2022). Linee guida per la classificazione e gestione del rischio, la valutazione della sicurezza ed il monitoraggio dei ponti esistenti. Rome, Italy. https://www.mit.gov.it/sites/default/files/media/notizia/2020-05/1_Testo_Linee_Guida_ponti.pdf.

Paar, G., Kontrus, H., 2006. Three-dimensional tunnel reconstruction using photogrammetry and lasers scanning. Proceedings of the 3rd Nordost, 9.

Pepe, M., Costantino, D., 2021. UAV photogrammetry and 3D modelling of complex architecture for maintenance purposes: The case study of the masonry bridge on the Sele river. Italy. Periodica Polytechnica Civil Engineering 65 (1), 191–203. https://doi.org/10.3311/PPci.16398.

Pinto, L., Bianchini, F., Nova, V., Passoni, D., 2020. Low-cost uas photogrammetry for road infrastructures'inspection. Int. Arch. Photogramm. Remote. Sens. Spat. Inf. Sci. 43, 1145–1150. https://doi.org/10.5194/isprs-archives-XLIII-B2-2020-1145-2020.

Salomone, R., Damiani, F., Vittone, M., Napolitano, M.S., Vangelisti, I., Giacalone, G., Beltrami, C., 2023. In: Visual Inspection of Bridges and Tunnels in Italy: by Experience Made with Different Owners and Methods to a New Proposal for a Better and More Efficient Inspection Procedures. CRC Press, pp. 3508–3515. https://doi.org/10.1201/9781003323020-429.

Scaioni, M., Barazzetti, L., Giussani, A., Previtali, M., Roncoroni, F., Alba, M.I., 2014. Photogrammetric techniques for monitoring tunnel deformation. Earth Sci. Inf. 7, 83–95. https://doi.org/10.1007/s12145-014-0152-8.

Soudarissanane, S., Lindenbergh, R., Menenti, M., Teunissen, P., 2011. Scanning geometry: Influencing factor on the quality of terrestrial laser scanning points. ISPRS J. Photogramm. Remote Sens. 66 (4), 389–399. https://doi.org/10.1016/j.isprsjprs.2011.01.005.

The MathWorks Inc, 2024. MATLAB version: 24.1.0 (R2024a). The MathWorks Inc, Natick, Massachusetts. https://www.mathworks.com.

Walton, G., Delaloye, D., Diederichs, M.S., 2014. Development of an elliptical fitting algorithm to improve change detection capabilities with applications for deformation monitoring in circular tunnels and shafts. Tunn. Undergr. Space Technol. 43, 336–349. https://doi.org/10.1016/j.tust.2014.05.014.

Weixing, W., Weiwei, C., Kevin, W., Shuang, L., 2020. Extraction of tunnel center line and cross-sections on fractional calculus, 3D invariant moments and best-fit ellipse. Opt. Laser Technol. 128, 106220. https://doi.org/10.1016/j.optlastec.2020.106220.

Xu, H., Wang, M., Liu, C., Li, F., Xie, C., 2024. Automatic detection of tunnel lining crack based on mobile image acquisition system and deep learning ensemble model. Tunn. Undergr. Space Technol. 154, 106124. https://doi.org/10.1016/j.tust.2024.106124.

Zollini, S., Alicandro, M., Dominici, D., Quaresima, R., Giallonardo, M., 2020. UAV photogrammetry for concrete bridge inspection using object-based image analysis (OBIA). Remote Sens. (Basel) 12 (19), 3180. https://doi.org/10.3390/rs12193180.